Microporous and Mesoporous Materials 379 (2024) 113301

Contents lists available at ScienceDirect

Microporous and Mesoporous Materials

journal homepage: www.elsevier.com/locate/micromeso

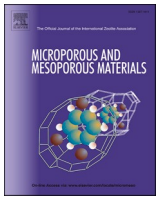

Evaluation of potential adsorbents for simultaneous adsorption of phosphate and ammonium at low concentrations

Uzma Shaheen [a,b], Zhi-Long Ye [a,c,*], Olusegun K. Abass [d,**], Doaa Zamel [a,b], Abdul Rehman [b], Peng Zhao [a,b], Fengming Huang [a,b]

[a] Key Laboratory of Urban Pollutant Conversion, Institute of Urban Environment, Chinese 905, Academy of Sciences, Xiamen, 361021, China
[b] University of Chinese Academy of Sciences, Beijing, 100049, China
[c] Fujian Key Laboratory of Digital Technology for Territorial Space Analysis and Simulation, Xiamen, 361021, China
[d] Department of Civil Engineering and ReNEWACT Laboratory, Landmark University, P.M.B 1001, Omu-Aran, Nigeria

ARTICLE INFO

Keywords:
Simultaneous adsorption
Low concentration
Ammonium
Phosphate
Nutrient recovery

ABSTRACT

Evaluation of potential adsorbents to tackle eutrophication caused by low concentrations of phosphate and ammonium are rarely reported in the literature. Besides, the dynamics/mechanisms for removal of these pollutants at low concentration are yet to be explored. In this study we used five different adsorbents, including La-modified zeolite (LMZ), MgFe-modified biochar (MgFe-BC), phoslock, activated alumina (AA), and diatomaceous earth (DE) to evaluate the removal of these pollutants. Among the selected adsorbents in this study, LMZ and AA both exhibited effective and simultaneous adsorption for phosphate and ammonium and the maximum adsorption capacities were 2.47 mg/g and 3.07 mg/g, respectively. The presence of SO_4^{2-} and CO_3^{2-} negatively impacted phosphate adsorption, while Fe^{3+} and K^+ ions inhibited ammonium adsorption. LMZ adsorption kinetics was over 3 times faster than other adsorbents within 60 min reaction time. Kinetics studies and isotherms revealed that the removal of phosphate and ammonium was primarily driven by chemical interactions and monolayer adsorption and were better fitted by Langmuir isotherm than the Freundlich isotherm and kinetic study was effectively described by Pseudo-second-order kinetic model. FTIR and XPS analysis revealed that the key mechanisms for phosphate adsorption were electrostatic attraction and inner sphere complexation through ligand exchange, whereas ammonium adsorption was mainly governed by ion exchange. Desorption study revealed that LMZ material was stable after three desorption cycles. This study offers vital knowledge on the nature of adsorption and interactions of potential mesoporous adsorbents with eutrophication-causing pollutants in lakes and rivers and proposes effective remedial mean.

1. Introduction

Water eutrophication poses a significant environmental concern and is mainly caused by phosphate and ammonium nutrients. These compounds are present in various wastewaters at different concentrations [1]. The Strict environmental standards outlined by the United States Environmental Protection Agency and China Ministry of Ecology and Environment specify stringent limits for phosphorus levels in surface water, aiming to maintain phosphorus concentrations below 0.02 mg/L and 0.5 mg/L. Even at concentrations slightly above 0.02 mg/L, because phosphate can trigger abnormal microbial growth which led to eutrophication [2,3]. Additionally, ammonium concentrations are advised to stay below 3 mg/L to preserve water quality [4]. Therefore, it's crucial pursuing suitable, affordable and environmentally sustainable techniques to eliminate low-concentrated phosphate and ammonium from eutrophic water.

For the purpose of regulating and reduce the concentration of phosphate and ammonium in contaminated water, significant research efforts have been directed towards developing effective and affordable technology capable of simultaneously mitigating these contaminants [5]. Conventional techniques for isolated removal of phosphate and ammonium have been developed, for instance ion exchange [6,7],

* Corresponding author. Key Laboratory of Urban Pollutant Conversion, Institute of Urban Environment, Chinese 905, Academy of Sciences, Xiamen, 361021, China.
** Corresponding author.
E-mail addresses: zlye@iue.ac.cn (Z.-L. Ye), abass.olusegun@lmu.edu.ng (O.K. Abass).

https://doi.org/10.1016/j.micromeso.2024.113301
Received 7 June 2024; Received in revised form 8 August 2024; Accepted 13 August 2024
Available online 15 August 2024

biological treatment [8], physicochemical [9], reverse osmosis [10] adsorption [11,12] and precipitation [13]. Adsorption is frequently considered the ideal technique because of its inexpensive cost, low energy usage, relatively simple implementation and environmentally friendly [7,14,15]. Additionally, the adsorption method is capable of eliminating biological, organic, and inorganic contaminants that are soluble or insoluble [16].

To develop efficient adsorbents for water treatment, significant research has been directed towards the utilization of commercial adsorbents such as carbon nanotubes, activated carbon, and graphene [17, 18]. These complexing adsorbents, while effective, are associated with high costs and require commercial-scale production [19]. In addition to synthetic materials, industrial byproducts, such as fly ash, wood, sawdust, attapulgite, oxide nanoparticles, and zero-valent iron are the main sources of these adsorbents. Other materials include clay minerals, zeolites, exfoliated vermiculites, fly ash, peats, and chitosan beads [14]. Although certain materials appear promising for the removal of phosphate and ammonium from water, achieving simultaneous and efficient elimination of these contaminants at low concentrations presents significant challenges [20]. For instance, clay-based materials options such as zeolite [21] and mesoporous silica-modified bentonite [22] form a diverse family of adsorbents known for their diverse native physicochemical attributes, including a large surface area and high cation exchange capacity, making them prominent in wastewater treatment applications [16].

For instance, research indicates that due to their negative charge, zeolites can effectively adsorb cationic pollutants from water. Studies have found that incorporating or impregnating metal oxides significantly enhances the phosphate adsorption capacity of adsorbents. Lanthanum-modified adsorbents, in particular, offer notable benefits over those modified with calcium, aluminum, or iron, including superior adsorption capacity, a broad pH range, and a high removal rate is 96 % for adsorption of phosphate. Previous research has not investigated the behaviors and mechanisms of simultaneously adsorbing ammonium and phosphate from wastewater using Lanthanum modified zeolite [23]. Other adsorbents including biochar have been used for phosphate and ammonium sequestration [24]. Fang et al. prepared Ca–Mg-modified biochar at different temperatures and noted that the composite with the highest modification temperature achieved the highest phosphate adsorption at 326.63 mg/g [25]. They further showed that phosphate adsorption on Ca–Mg biochar was not significantly influenced by changes in the pH of the biogas fermenting fluid. Activated alumina have shown potential to act as both an efficient adsorbent and a porous substrate depending on its application [17,26]. However, previous research has demonstrated that the relatively low specific surface area of alumina-based adsorbents leads to inadequate adsorption capacity. Prior to this report, several adsorbents previously used in the literature to remove phosphate and ammonium individually at high concentrations, such as ca-modified biochar, mg-modified biochar [25,27] and activated carbon [28] were ineffective to reduce the pollutants when utilized at low concentration.

Thus, in this study, five previously reported adsorbents including LMZ, MgFe-BC, phoslock, AA, and DE [23,29–32], were utilized for simultaneous adsorption of phosphate and ammonium at low concentrations. Besides, we focused on the kinetics and adsorption capacities of the adsorbents. We also investigate the effect of coexisting ion on simultaneous adsorption of phosphate and ammonium. This work represents a new focus in the field and offers crucial insights into the fundamental principles governing adsorption interactions among various adsorbents at low concentration phosphate and ammonium eutrophic waters.

2. Materials and methods

2.1. Materials

In this work, five different materials, including rice straw biochar, bentonite, zeolite, activated alumina, and diatomaceous earth, have been investigated. The rice straws, bought from Jiangsu, Lianfeng Agricultural Products Deep Processing Company, China. Commonly used activated alumina (AA) and diatomaceous earth (DE) were commercially obtained and used without extra preparation.

Chemically pure agents, including $FeCl_3{\cdot}6H_2O$, $MgCl_2{\cdot}6H_2O$, $LaCl_3$, $La(NO_3)_3{\cdot}6H_2O$, NH_4Cl, and KH_2PO_4, were obtained as analytical grade from Sinopharm Chemical Reagent Co., Ltd., China. Standard solution of phosphate and ammonium were prepared was prepared by dissolving KH_2PO_4 and NH_4CL in deionized water.

2.2. Preparation and fabrication of adsorbents

MgFe modified Biochar (MgFe-BC); was prepared via the co-pyrolysis of biomass and magnesium and iron using the following procedure. First, 10 g of purified straw were placed in 500 mL beaker of deionized (DI) water. Next, 10.28 g of $MgCl_2$ and 4.77 g of $FeCl_3{\cdot}6H_2O$ were placed into the beaker with the rice straw, and the mixture was continuously stirred at 60 °C. The mixture was subsequently washed repeatedly with DI water and filtered, then was placed in an oven at 60 °C overnight. The resulting mixture was poured into a mortar and pulverized. Finally, the dried sample was inserted into a muffle furnace and pyrolyzed at 600 °C for 2 h under a nitrogen atmosphere [24].

Lanthanum modified zeolite (LMZ); firstly, 10 g of natural zeolite were added to a solution of 1.25 g of lanthanum chloride mixed into 50 mL of DI water. After this then the mixture was agitated for 3 h at 60 °C. Next, the mixture was placed in a drying oven for 12 h at 80 °C. Then the particles of zeolite were subsequently washed with DI water [33].

Lanthanum modified bentonite (Phoslock); Co-precipitation technique was used in preparing of the La modified bentonite. The process involved mixing 4 g quantity of bentonite in 50 mL of deionized water using a magnetic stirrer. Then, 2 g of lanthanum carbonate were added to the mixture, which was subjected to magnetic stirring for 6 h. After 6 h of stirring, white sediments formed. After several rinses, the particles were dried and prepared for further use. This adsorbent is known as Phoslock after modification [34].

2.3. Adsorption experiments

2.3.1. Effect of adsorbents dosage on phosphate and ammonium removal

To investigate the effect of different amount of adsorbent dosage on the adsorption of phosphate and ammonium, tests were carried out by combining specific dosages of 0.1–1.5 g/L of adsorbent with 250 mL of phosphate and ammonium solution to achieve phosphate with 1 mg/L and ammonium with 5 mg/L, respectively. Since the ideal pH range for adsorption has already been established by previous studies, pH optimization was not conducted independently in this investigation. We adjusted the pH to 7 based on these established findings and the results reported in existing literature [35]. Ammonium concentration was measured using a spectrophotometric method with Nessler's reagent at 420 nm utilizing a UV-9000IC METASH spectrophotometer. Phosphate levels were assessed via the ascorbic acid-ammonium molybdate spectrophotometric method at 700 nm. Each experiment was conducted in triplicate. The removal efficiency (R, %) was calculated as follows:

$$\boldsymbol{R} = \frac{(\boldsymbol{C_0} - \boldsymbol{C_f})\mathbf{100}}{\boldsymbol{C_0}} \tag{1}$$

where C_0 (mg/L) represent the initial phosphate and ammonium concentrations and C_f (mg/L) indicates the final concentration of phosphate and ammonium at equilibrium stage.

2.3.2. Adsorption equilibrium

The experiments of adsorption capacity were conducted by varying the initial phosphate concentrations at 0.5, 1, 1.5, 2, and 2.5 mg/L, and ammonium concentrations at 1, 3, 5, 6, 10, and 20 mg/L, respectively, in 250 ml of water. The adsorption capacity (Q_e, mg/g) were estimated as follows of phosphate and ammonium:

$$\boldsymbol{Q_e} = \frac{(\boldsymbol{C_0} - \boldsymbol{Ce})\boldsymbol{V}}{\boldsymbol{m}} \tag{2}$$

Where, C_0 and C_e (mg/L) represent the initial and equilibrium concentrations of phosphate and ammonium; m (g) denotes the adsorbent mass and V (L) represents volume of adsorption solution.

2.3.3. Adsorption kinetics

Experiments to investigate kinetic adsorption were conducted, utilizing initial concentrations of phosphate and ammonium set at 1 mg/L and 5 mg/L, respectively, in 1000 ml of water. Every experiment was conducted three times, and the mean was determined. The adsorption capacity at various times t (Q_t, mg/g) were estimated as follows:

$$\boldsymbol{Q_t} = \frac{(\boldsymbol{C_0} - \boldsymbol{C_t})\boldsymbol{V}}{\boldsymbol{m}} \tag{3}$$

Where, where Qt (mg/g) indicates the adsorption capacity of phosphate and ammonium at time t, respectively; C_0 and C_t (mg/L) represent the initial and final concentrations of phosphate and ammonium at time t, respectively; m (g) denotes the mass of adsorbent and V (L) representing the volume of the solution.

2.3.4. Effects of co-existing ions

The effects of coexisting anions and cations effects was also investigated. In this study, three common anions, i.e., Cl^-, SO_4^{2-}, and CO_3^{2-}, and three common cations, Na^+, Fe^{3+}, and K^+ at equal molar concentrations were selected and prepared by mixing KH_2PO_4 and NH_4Cl (1, 5 mg/L) with anions or cations set at an equal molar ratio of 1:1.

2.3.5. Desorption study

In order to achieve reuse of the adsorbent, the most efficient adsorbent was selected for the desorption process. Phosphate and ammonium absorbed unto optimized adsorbent were removed using a method similar to the one described in above adsorption experiment, employing a 1 M NaOH solution. Subsequent to agitation, the solution was examined to determine the amounts of ammonium and phosphate. Furthermore, the optimized adsorbent underwent rinsing with DI water and then was dried, resulting to the production of the desorbed adsorbent. Subsequently, this adsorbent was utilized for the subsequent adsorption test. This process was repeated three times.

2.4. Characterization

The surface characteristics of the adsorbents were examined with an electron microscope (SEM, S-4800, Hitachi, Japan). The crystalline structures of adsorbents were examined with an XRD-X'Pert PRO instrument (Panalytical, The Netherlands). The Fourier transform infrared spectroscopy (FTIR, Thermo Scientific Nicolet iS10, USA) was used to analyze the adsorbents chemical composition. Moreover, X-ray photoelectron spectroscopy (XPS) spectra were obtained using a PHI Quantum-2000 electron spectrometer (Ulvac-Phi, Japan) to determine the surficial chemical states of the adsorbents. Before characterization, all the materials were subjected to drying in an oven at 40 °C for duration of 24 h.

2.5. Adsorption model fitting

Langmuir and Freundlich isotherm equations were utilized to estimate the adsorption behavior of each adsorbent.

Langmuir equation

$$q_e = q_{max}\frac{K_l C_e}{1 + K_l C_e} \tag{4}$$

Freundlich equation

$$q_e = K_F Ce^{1/n} \tag{5}$$

Where, qm signifies the maximum adsorption capacity (mg/g); qe refers to the equilibrium adsorption capacity (mg/g); and Ce represents the equilibrium concentration. K_L is the affinity constant and K_F indicates the Freundlich constant, while n denotes the Freundlich isothermal variation pattern.

The Pseudo-first-order (PFO) and pseudo-second-order (PSO) kinetic equation models were concurrently utilized to investigate the adsorption mechanisms of phosphate and ammonium on the five distinct adsorbents [36].

Pseudo-first-order kinetic model equation:

$$q_t = qe(1\text{-}e_1^{tk}) \tag{6}$$

Pseudo-second-order kinetic model equation

$$q_t = \frac{(\mathbf{k2q2\ et})}{\mathbf{1 + k2qet}} \tag{7}$$

Where, q_t and q_e (mg/g) represents the quantity of phosphate and ammonium adsorbed at the given time; k_1 (min^{-1}) and k_2 (g/mg/min) are the rate constants of the pseudo-first-order and pseudo-second-order kinetic equations, respectively.

3. Results and discussion

3.1. Simultaneous adsorption capability

3.1.1. Effect of different adsorbent dosages on phosphate and ammonium removal

F ig. 1a and b describe the adsorption capacities of the adsorbents for simultaneous adsorption of ammonium and phosphate. It was found that with the increase of quantity of adsorbent from 0.1 to 1.5 g, phosphate removal efficiency increased significantly (Fig. 1a). On one hand, a stabilization in the removal efficiency was observed at different adsorbent dosages greater than 1 g. This phenomenon was caused by more adsorption sites for phosphate being available at higher adsorbent dosages. Nonetheless, increasing the dose beyond 1 g did not substantially enhance efficiency. This was because the adsorbate adsorption was strongly dependent on the existence of active sites for adsorption on the adsorbents surface alongside the concentration of phosphate in the water. In addition, AA exhibited the highest removal efficiency at 95.10 %, indicating its exceptional efficiency in removing phosphate from the solution. Whereas, phoslock followed closely with a removal efficiency of 90.20 %, showcasing substantial phosphate removal capabilities. LMZ demonstrated a significant adsorption capacity of 75.26 %. On the other hand, MgFe-BC and DE showed lower adsorption capacities of ammonium and phosphate compared to those three adsorbents.

As for ammonium, LMZ exhibited the highest adsorption capacity at 75.44 %, as shown in Fig. 1b. Incorporating additional adsorbent material leading to rise in both number of ion-exchange areas and the adsorption surface areas on the zeolite [37]. Conversely AA, MgFe-BC, phoslock, and DE demonstrated lower adsorption capacities for ammonium compared to LMZ. To reason for the higher adsorption capacity performance of LMZ is elucidated in the following sections.

Nevertheless, an increased dose of more than 1g did not significantly impact the removal efficiency. The rationale behind this was that the adsorbent ability to adsorbed phosphate and ammonium was heavily dependent on the existence of an active adsorption site onto the surface of the adsorbent and the concentration of phosphate and ammonium in the aqueous medium as well [38]. In addition, the extent of active sites

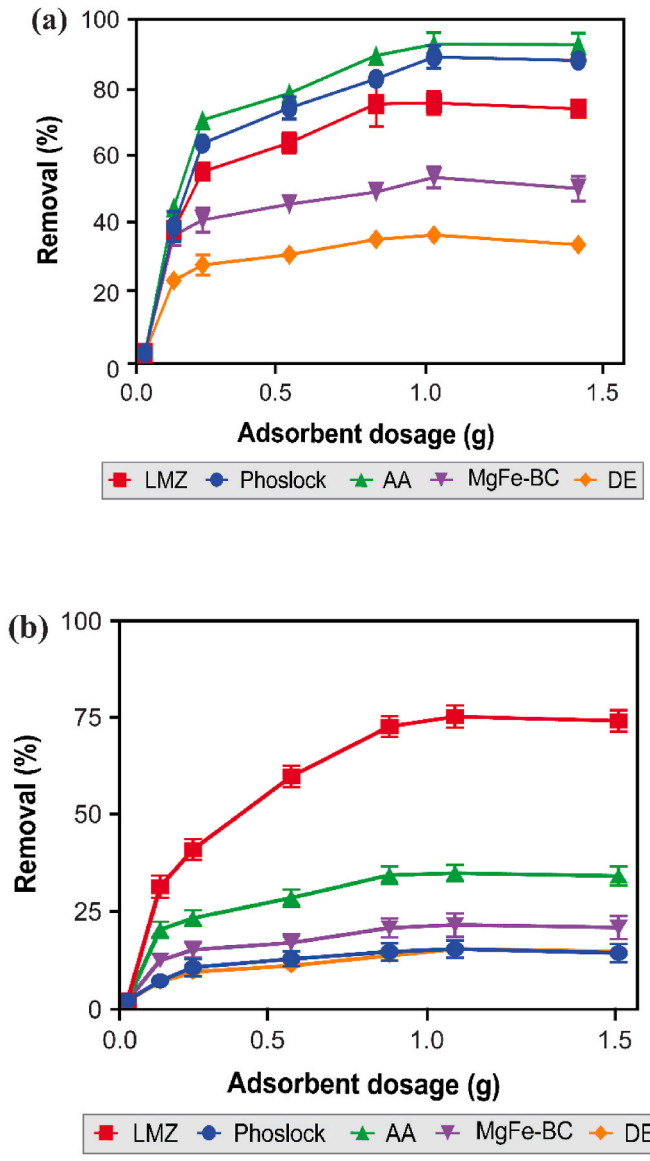

Fig. 1. Effects of different adsorbent dosages on co-adsorption of (a) phosphate and (b) ammonium (*dosage 0-1.5 g, initial concentration of phosphate* = 1 mg/L, *phosphate* = 5 mg/L, *time 8 h,* pH = *7*). Data are provided as mean ± SD (*n* = 3).

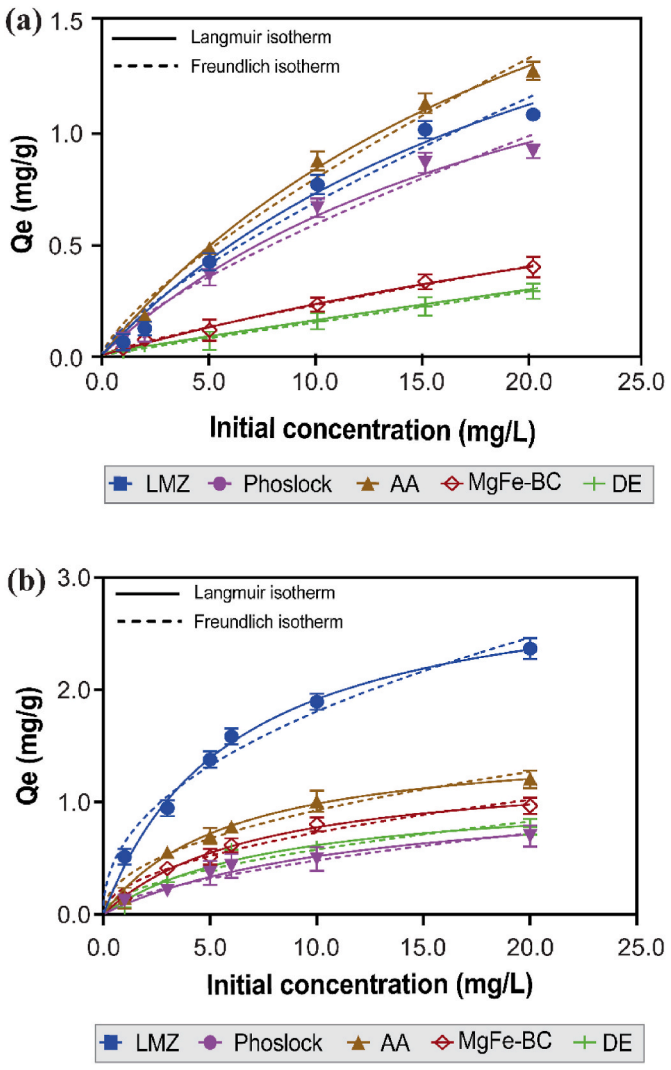

Fig. 2. Adsorption isotherm (a) phosphate and (b) ammonium (*dosage 1 g, time 8 h, initial concentration of phosphate* = *1 to* 2 mg/L, *ammonium* = *5 to* 20 mg/L, pH = *7*). Data are provided as mean ± SD (*n* = 3).

was greater than the amount of available phosphate in the aqueous medium at higher doses, which also leading to a decline in the adsorption capacities [39]. Phoslock, LMZ, and AA showed significant efficiency in removing phosphate. Conversely, their capability to remove ammonium was noticeably limited. Notably, LMZ exhibited remarkable effectiveness to sufficiently remove both phosphate and ammonium simultaneously relative to other adsorbents used.

3.1.2. Adsorption equilibrium of phosphate and ammonium

The analysis of adsorption isotherms was conducted using concentrations of phosphate at 0, 0.5, 1, 1.5, 2, and 2.5 mg/L, and ammonium concentrations at 0, 1, 3, 5, 6, 10, and 20 mg/L, respectively.

As demonstrated in Fig. 2a and b, phosphate and ammonium adsorption capacities increased on all adsorbents in relation to the initial concentration level, and these capacities then gradually stabilized. Table 1a and b demonstrate that, in comparison to the Freundlich, the appropriate fitting correlation of coefficients of all adsorbents for phosphate and ammonium within the Langmuir equation contained a marginally higher value of $R^2 > 0.96$. The phosphate and ammonium

Table 1a
Parameters of co-adsorption isotherm for phosphate adsorption by every adsorbent (*dosage* 1 mg/L, *time 8 h, initial concentration of phosphate* = *1 to* 2 mg/L).

Adsorbent type	Langmuir isotherm			Freundlich isotherm		
	Q_{max} (mg/g)	K_L (mg/L)	R^2	n	K_F (mg/L)	R^2
LMZ	2.470	0.4223	0.9854	0.6866	1.328	0.9726
Phoslock	2.033	0.4410	0.9815	0.5873	1.245	0.9682
AA	2.901	0.4039	0.9941	0.7925	1.332	0.9854
Mg-Fe-BC	1.440	0.2008	0.9623	0.2246	1.214	0.9624
DE	0.587	0.0377	0.9391	0.1478	1.047	0.9391

adsorption behaviors can be more accurately represented by the Langmuir equation. According to earlier studies, the adsorption is generally monolayer in framework [40], which means that the adsorbed materials were uniformly dispersed across the adsorbent's surface to reach saturation [41].

Additionally, Table 1a and b also showed that AA, LMZ, and phoslock had maximum adsorption capacities for phosphate, with values of 2.90, 2.47 and 2.03 mg/g, respectively. Though, phoslock, LMZ, and AA demonstrated a strong adsorption impact on phosphate, their adsorption

Table 1b
Parameters of co-adsorption isotherm for ammonium adsorption by every adsorbent (*dosage 1 g, time 8 h, initial concentration of ammonium = 5 to* 20 mg/L, pH = *7*).

Adsorbent type	Langmuir isotherm			Freundlich isotherm		
	Q_{max} (mg/g)	K_L (mg/L)	R^2	n	K_F	R^2
LMZ	3.075	0.1706	0.9889	0.6553	2.256	0.9724
Phoslock	1.173	0.0764	0.8819	0.1163	1.629	0.8619
AA	1.560	0.1718	0.9710	0.3256	2.199	0.9369
Mg-Fe-BC	1.367	0.1302	0.9711	0.2248	1.965	0.9378
DE	1.108	0.1258	0.9553	0.1750	1.926	0.9205

performance on ammonium was poor except for LMZ that demonstrates remarkable ammonium removal characteristics (3.07 mg/g), which was effective for the adsorption of both ammonium and phosphate.

3.1.3. Adsorption kinetics of phosphate and ammonium

Fig. 3a and b presents the adsorption kinetics of ammonium and phosphate on five distinct adsorbents. Wherein the adsorption capacities of LMZ, phoslock, AA, MgFe-BC, and DE for phosphate increased quickly during the first 10 min of adsorption and then slowed down 5–480 min later until they reached equilibrium. The adsorption capacities remained almost unchanged after 480 min. Furthermore, there were variations in the equilibrium times of ammonium adsorption on adsorbents. For example, LMZ adsorption increased quickly in the first phase (0–60 min) and then becomes steady prior to reaching a state of equilibrium from 60 to 380 min. Conversely, the adsorption capacities of phoslock, AA, MgFe-BC, and DE increased steadily during the first stage (0–10 min) at a very slow rate of adsorption. However, the existence of a relationship between the duration of time and the adsorption capacities of ammonium and phosphate on the five different adsorbents showed a similar pattern of increase at initial stages before trending toward equilibrium. The equilibrium level for ammonium and phosphate was reached after 480 min of reaction. Thus, the testing period for adsorption was determined to be 480 min.

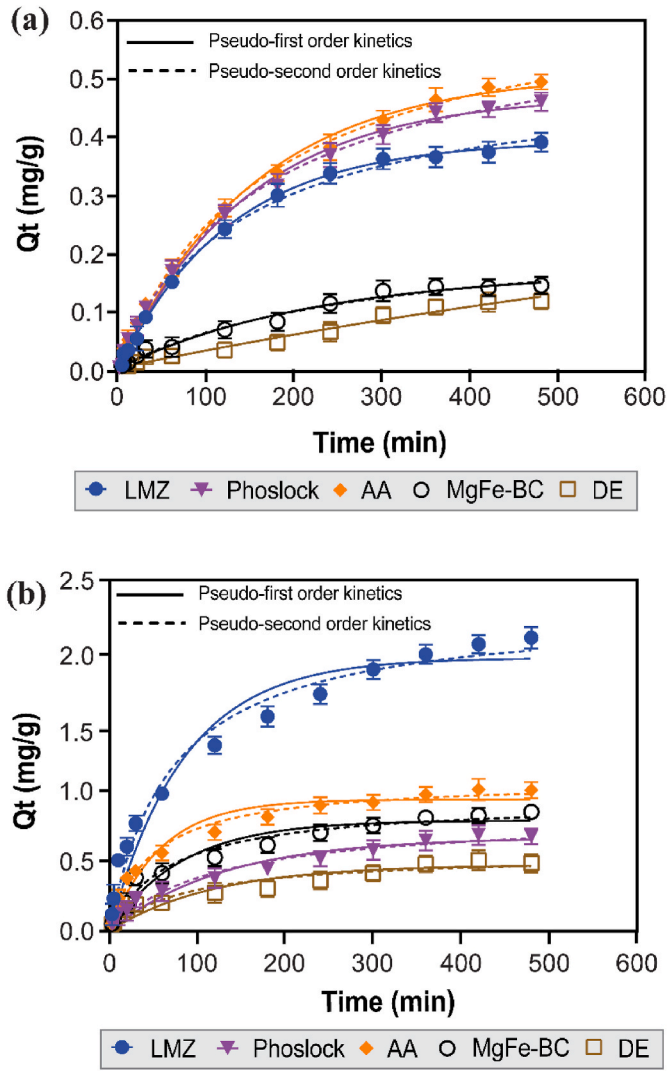

Fig. 3. Adsorption kinetics of (a) phosphate and (b) ammonium (*dosage* 1 g/L, *time 8 h, initial concentration of* ammonium = 5 mg/L, phosphate = 1 mg/L, pH = *7*). Data are provided as mean ± SD (*n* = 3).

To pursue further inquiry into the mechanisms of adsorption, the kinetic behaviors of phosphate and ammonium were examined by using the PFO and PSO models, based on the experimental results. The findings and correlation coefficients were shown in Table 2a and b. Both models fit the kinetic data for these adsorbents quite well and thorough comparison of the R^2 values indicated that the PSO model better represented the kinetic data for these adsorbents (all >0.99). This suggests that the PSO model provides a more accurate depiction of the adsorption process. In contrast with the other adsorbents, LMZ simultaneously adsorbs both phosphate and ammonium, with maximum Qt values of approximately 0.5 mg/g for phosphate and 2.2 mg/g for ammonium. The adsorption process for LMZ is rapid initially and reaches equilibrium gradually, fitting well with the PSO. Phoslock shows notable capacity, reaching Qt values near 0.6 mg/g for phosphate, following a kinetic pattern similar to LMZ and fits well with the PSO model. AA demonstrates considerable adsorption capacity, achieving a maximum Qt of about 0.6 mg/g for phosphate, exhibiting kinetics similar to LMZ and Phoslock.

In contrast, MgFe-BC exhibits lower adsorption capacity compared to LMZ, Phoslock, and AA, with Qt values around 0.1 mg/g for phosphate. The PSO model fits both pollutants better than the pseudo-first-order model, although its adsorption process is slow and reaches equilibrium late. Among the adsorbents, DE has the lowest adsorption capacity; its maximum Qt values for phosphate are around 0.1 mg/g. The PSO model fits the experimental data better than the PFO model, and the adsorption kinetics for DE are similar to those of the other adsorbents in that equilibrium is achieved more slowly. Overall, the adsorption capacities for phosphate follow the order: AA > Phoslock > LMZ > MgFe-BC > DE, while for ammonium they follow: LMZ > AA > MgFe-BC > Phoslock > DE. All adsorbents and pollutants perform better with the PSO model, indicating their unique physicochemical characteristics, including functional groups, surface area, pore structure. Thus, the adsorption of phosphate and ammonium was mainly controlled by chemical adsorption, which could potentially include complexation and electrostatic interactions [42–44].

Nonetheless, the process-controlling step may be the porosity of the adsorbent particles, which allows an adsorbate to enter through its inner layer and regulate the adsorption rate.

Table 2a
Kinetic parameters for phosphate co-adsorption by every adsorbent (*dosage* 1 g/L, *time 8 h, initial concentration of phosphate* = 1 mg/L).

Adsorbent type	Pseudo-first kinetic order			Pseudo-second kinetic order		
	Q_e (mg/g)	k_1 (min^{-1})	R^2	Q_e (mg/g)	k_2 (min^{-1})	R^2
LMZ	0.3881	0.0079	0.9931	0.5032	0.4793	0.9942
Phoslock	0.4662	0.0068	09914	0.6106	0.5824	0.9937
AA	0.5039	0.0064	0.9916	0.6649	0.6343	0.9944
MgFe-BC	0.1652	0.0044	0.9524	0.2374	0.1971	0.9517
DE	0.1466	0.0086	0.9423	0.6607	0.1022	0.9582

Table 2b
Kinetic parameters for ammonium co-adsorption by each adsorbent (*dosage* 1 g/L, *time 8 h, initial concentration of* ammonium = 5 mg/L, pH = *7*).

Adsorbent type	Pseudo-first kinetic order			Pseudo-second kinetic order		
	Q_e (mg/g)	k_1 (min^{-1})	R^2	Q_e (mg/g)	K_2 (g/mg/min)	R^2
LMZ	1.946	0.0118	0.9562	2.289	2.169	0.9773
Phoslock	0.6679	0.0077	0.9255	0.8196	0.726	0.9391
AA	0.9382	0.0171	0.9558	1.0760	1.030	0.9774
MgFe-BC	0.7749	0.0089	0.9368	0.9369	0.851	0.9521
DE	0.4731	0.0084	0.8475	0.5496	0.417	0.8733

3.1.4. Effect of co-existing ions on phosphate and ammonium adsorption capacity

Natural water and wastewater are often characterized by high concentrations of anions and cations, which compete with phosphate and ammonium for the active sites on the adsorbents. Consequently, it is necessary to evaluate the possible impact of concurrent ions on the ammonium and phosphate adsorption of every adsorbent. In the context of the current study, three common anions (Cl^-, SO_4^{2-}, and CO_3^{2-}) and three common cations (Na^+, Fe^{3+}, and K^+) at equal molar concentration were selected as co-existing anions and cations. The experimental findings are demonstrated in Fig. 4a and b, where monovalent anions (Cl^-) and cations (Na^+, Fe^{3+}, and K^+), did not reduce the adsorption efficiency of phosphate compared to the blank runs.

In Fig. 4a, the phosphate adsorption capacity is slightly reduced in the presence of anions (Cl^-) and cations (Na^+, Fe^{3+}, and K^+). However, the occurrence of divalent anions namely SO_4^{2-} and CO_3^{2-} leading to a substantial decrease in the adsorption capacity of every adsorbent, with percentage changes of 3.55, 415.1, 32.05, 6.31, 6.91, and 42.38, 36.97, 26.05, 11.14, and 8.20 %, respectively. It is possible that this inhibition resulted from divalent anions stronger ionic strength and prolonged competition with monovalent anions for the adsorbents active sites [39]. Similarly, in Fig. 4b, ammonium removal was not affected by anions like Cl^-, CO_3^{2-} and SO_4^{2-}, as well as the cation Na^+. However, Fe^{3+}, and K^+ had a significant impact, with percentage changes of 4.72, 1.02, 1.41, 1.62, 1.63, and 4.1, 1.85, 1.81, 1.63, and 1.28 %, respectively. This implies that the adsorption method is more influenced by Fe^{3+}, and K^+. Additionally, K^+ and Fe^{3+} may be able to compete for adsorption sites with ammonium ions [45].

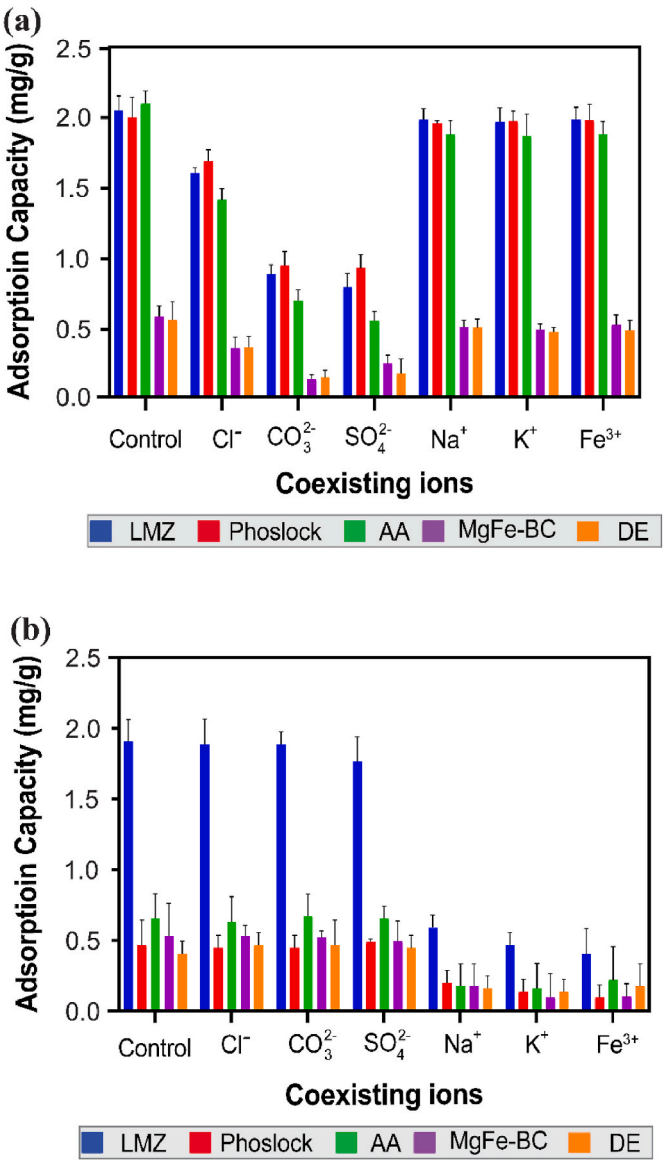

Fig. 4. Effect of coexisting ions effect on the co-adsorption capacities of (a) phosphate and (b) ammonium (b) (*dosage 1 g, time 8 h, initial concentration of phosphate* = 1 mg/L, ammonium = 5 mg/L, pH = *7*). Data are provided as mean ± SD (n = 3).

3.2. Characterization of adsorbents

3.2.1. Morphological characterization of adsorbents (SEM)

The morphological diagrams of LMZ, Phoslock, AA, MgFe-BC, and DE both before and after the adsorption was investigated using SEM and are displayed in Fig. 5A –J. As a result, the SEM images in Fig. 5A and B, indicated that the LMZ microcube surfaces were covered in flake-like particles after adsorption compare to the pristine LMZ. This change is likely due to the formation of a lanthanum phosphate complex as also reported by Yang et al., [46]. Moreover, multiple lumps established an arrangement of stacks that minimized the size of the intra-particle void. The physical shape of molecules on LMZ changed, and this is an indication of the phosphate and ammonium adsorption, which may be crystallized on the sites of LMZ and enlarged the particle.

The phoslock showed a coarse and porous surface, as indicated by SEM micrographs of the sample in Fig. 5C and D. It was obvious that a significant amount of nanoflakes were deposited on the adsorbent surface. The synchronized distribution of La and P in an unoccupied section suggests that $LaPO_4$ precipitation should be involved in the phosphate adsorption. The surface of AA had a rich porous structure prior to adsorption; however, it was uneven and rough after the adsorption, as displayed in Fig. 5E and F. On the other side, the MgFe-biochar surface was sharp, flat, and curved inwards, possessing a specific tiny number of microholes strewn throughout. This morphology was ascribed to the increased degree of disorder in the sheets due to the initial metal hydroxides contracting and wrapping, which are a result of dehydration and dihydroxylation throughout the pyrolysis process, as shown in Fig. 5G and H. Large crystals have been developed on the biochar surface after the adsorption process; therefore, the surface became more rough and the original pore framework was eliminated [24]. Fig. 5I and J illustrates the morphology of the DE, which is cylindrical and covered in a variety of hard forms and macropores.

3.2.2. Structural properties of adsorbents (XRD)

X-ray diffraction was performed for the detailed analysis of the crystalline structural arrangement and phase configuration of the studied material. As depicted in Fig. 6, the major zeolite peak for diffraction emerged at 21.65°, which indicated the existence of SiO_2 (PDF#31-0026) [35]. Diffraction peaks of 16.04°, 27.06°, 37.72°, and 47.29° appeared in LMZ, which turned out to be $La(OH)_3$ distinctive peaks (PDF#43–0784). Thus, it can be assumed that $La(OH)_3$ was the

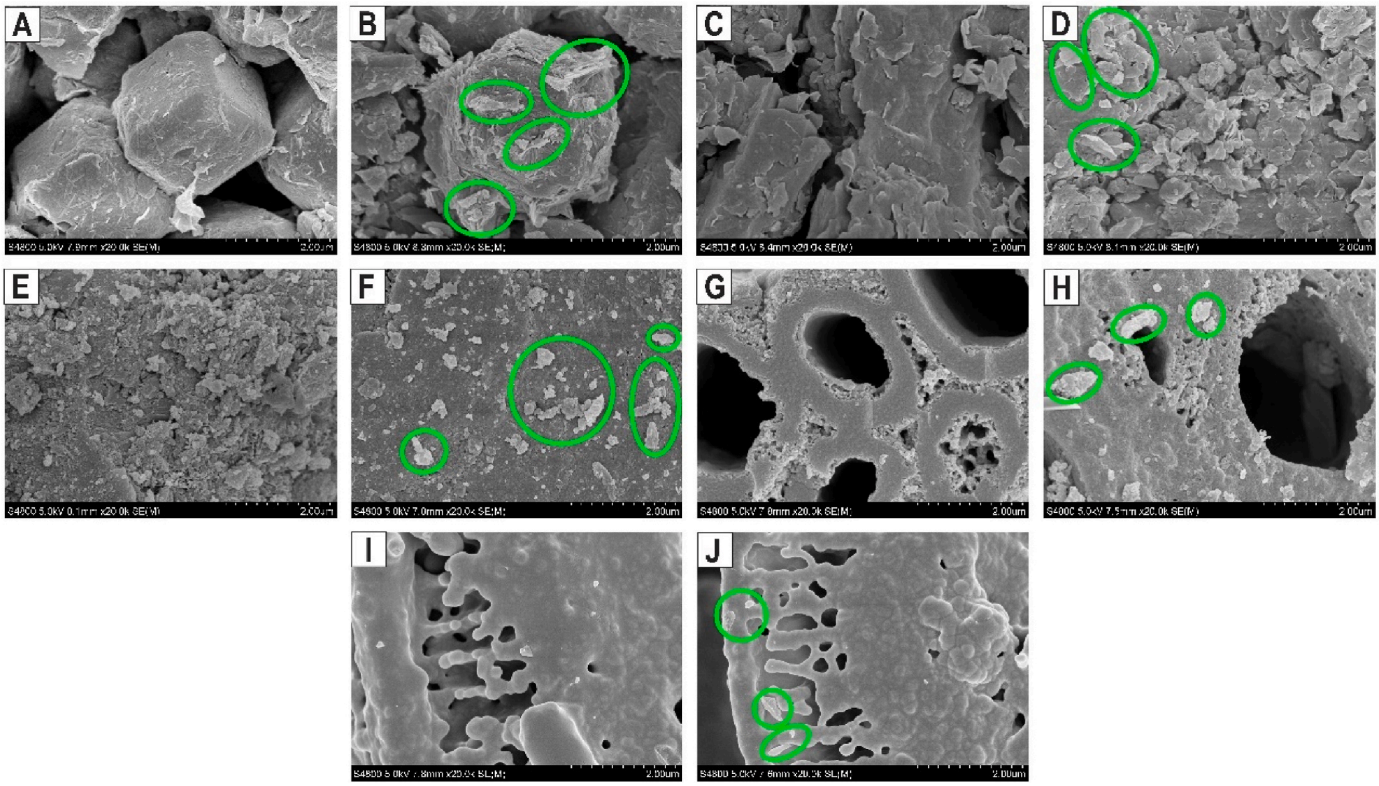

Fig. 5. SEM images before and after adsorption of (A and B) lanthanum modified zeolite, (C and D) phoslock, (E and F) activated alumina, (G and H) MgFe-biochar, and (I and J) diatomaceous earth.

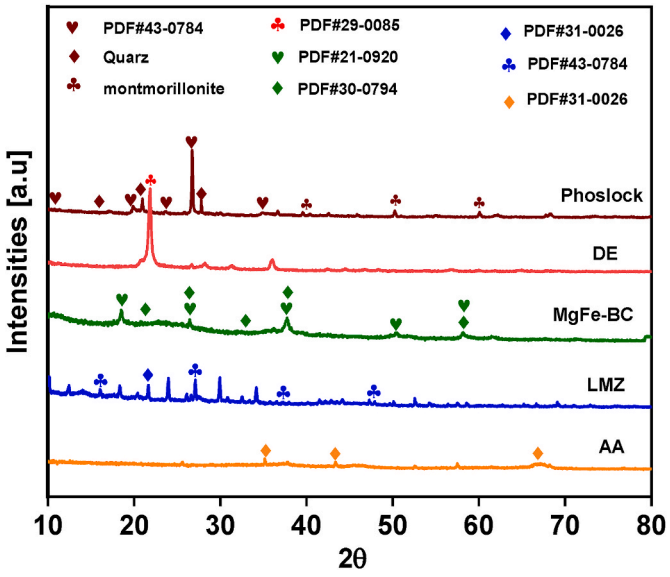

Fig. 6. XRD patterns before adsorption, lanthanum modified zeolite (LMZ), phoslock, activated alumina (AA), MgFe-biochar (MgFe-BC), and diatomaceous earth (DE).

lanthanum compound positioned on the LMZ surface [33]. Due to lanthanum modification, the predominant components were quartz (Qz) and montmorillonite (Mt), with a few weak peaks emerging as a result of the contaminants [29]. The characteristic peaks of the spectra of phoslock showed that lanthanum carbonate octahydrate was formed. Typically, peaks at 10.60°, 20.30°, 23.62°, 26.74°, and 34.99° correspond to $La_2(CO_3)_3{\cdot}8H_2O$ (PDF#43–0784) [34]. Minor peaks in (Fig. 6) may have been caused by layers in samples of phoslock adsorbent resulting from different lanthanum-related sources (such as $La(OH)_3$ and $LaCO_3OH$) [47].

The XRD of AA is further shown in (Fig. 6) it was found that metallic aluminum is characterized by peaks of diffraction at 2θ values of 67.19°, while AA is represented by the peaks at 35.13° and 43.3° (PDF#31-0026) [30]. Further analysis of the chemical composition and crystallinity was conducted via X-ray diffraction. From XRD data, it is evident that MgFe-BC has an amorphous composition because of its diffraction pattern, which lacks crystalline peaks. There were peaks in the MgFe-BC at 18.50°, 21.18°, 26.38°, 33.09°, 37.72°, 50.38°, and 58.18° (PDF#21–0920) (PDF#29–0085), and this represents a normal peak for MgO and Fe_2O_3. These results showed that the MgFe-BC had been prepared successfully [24,48]. The XRD profile of DE in Fig. 6 indicated that the material has some crystal structures and is slightly amorphous. Furthermore, the XRD analysis of DE showed a peak at 21.86°, which corresponds to cristobalite in the DE segment (PDF#29–0085) [49].

3.2.3. *Chemical compositional characteristics of adsorbents (FTIR)*

Fig. 7 demonstrates FTIR spectra analysis to further investigate the chemical composition of functional groups both before and after ammonium and phosphate adsorption. The tensile vibrations of the P–O bond in $H_2PO_4^-$ or HPO_4^{2-} and the O–P–O spectral vibrations in phosphate were observed at 1008.5 cm^{-1}, and 641.6 cm^{-1} confirming that the phosphate was effectively adsorbed onto LMZ. Moreover, the significant weakening of the –OH resonance peak at 3464.7 cm^{-1} indicated that the –OH was replaced by a La–O–P surface complex, while the band at 1602.0 cm^{-1}, may be due to the bending of the adsorbed water [50]. The group La–O–P identified at 510.2 cm^{-1} provided additional confirmation of ligand exchange occurring in the modified phosphate biochar [23,51]. Meanwhile, after the ammonium adsorption, a new peak at 1434.6 cm^{-1} corresponding to the symmetric stretching vibrations of N–H appeared, suggesting that ammonium removal onto LMZ occurred

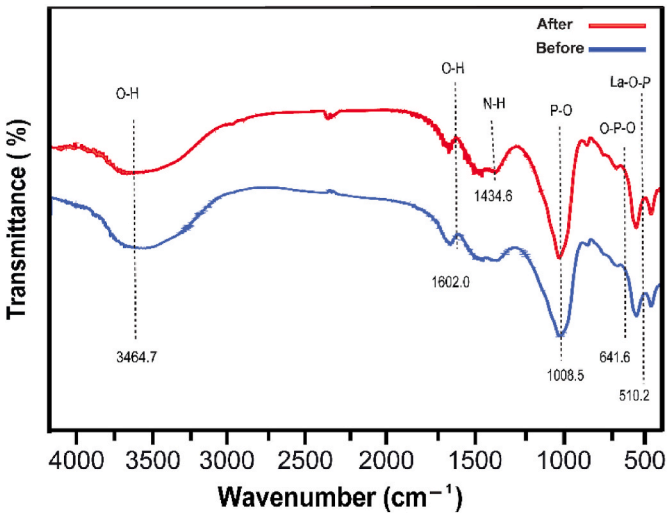

Fig. 7. FTIR analysis of adsorbents before and after adsorption of lanthanum-modified zeolite.

mainly through chemisorption. While, the retention of NH_4^+ on LMZ was primarily due to La^+ ion exchange ability, where La^+ exchanged with NH_4^+ in the aqueous medium [23,33]. The efficient removal mechanism of NH_4^+-N was due to ion exchange with La^+ in LMZ. For phosphate, the removal mechanisms included electrostatic adsorption, the generation of inner-sphere La–O–P complexes through ligand exchange.

The Si–O–Si antisymmetric vibration caused by stretching is represented by a strong peak at 1042 cm^{-1}, and the symmetrically stretching vibration of Si–O is represented by solid peaks at 796 cm^{-1} to 474 cm^{-1}, according to phoslock FTIR spectra in Fig. S1a [52]. This might be the result of montmorillonite, the primary mineral composition of phoslock. This material is composed of a pair of layers of aluminum surrounding a silicon-oxygen tetrahedron. The O–H bond was represented by peak values at 3738 cm^{-1}, 3634 cm^{-1}, 1710 cm^{-1}, and 1642 cm^{-1}. Among these instances, minerals were responsible for the peaks at 3634 cm^{-1} and 3738 cm^{-1} [53]. Conversely, the peaks at 1642 cm^{-1} suggested that the water molecules O–H bonds were present [34].

For AA, the wide range of adsorption near 3420.76 cm^{-1}, may be related to the intramolecular bonds of hydrogen and the O–H extending of water molecules that are absorbed, as indicated in Fig. S1b. The bands detected at 2396.76 cm^{-1} r result from the stretching of the –CH vibrations which includes $–CH_3$ and $–CH_2$ groups, both symmetrically and asymmetrically. The bending of the Al–OH framework is the cause of the vibration of AA at 1620 cm^{-1}. In addition, Al–O–Al bent and stretching vibrations are detected in the AA spectrum at 1039.06 cm^{-1} and 867.09 cm^{-1}, with a slight change in comparison with pure AA [17].

In Fig. S1c the FTIR results revealed the MgFe-BC noticeable peaks. The wide peak ranges among 3728 and 3448 cm^{-1} are expected to be due to vibrations from stretching of the interlayering of water-bonded hydroxyl group molecules. Additionally, there was extra crystalline water, or physisorbed water, in the close to single-bond hydrogen groups. The C=C group, the bond between layers of water, and the vibrations caused by the bending of the metallic hydroxides group of –OH are all represented by the peak at approximately 1567.9 cm^{-1} [54]. The brucite-type layers metal-oxygen as well as metal-oxygen-metal modes of vibration are represented by the low-frequency bands (below 1000 cm^{-1}) [54,55] showing that during the enhanced process, effective co-precipitation of MgFe-BC took place on the surface of the rice stover. Fig. S1d represents the FTIR spectra of DE. The FTIR analysis of DE revealed the vibrations caused by bending of the Si–O–Si categories at 478 and 620 cm^{-1}, a symmetrical stretching extended vibration of the Si–O group at 846 cm^{-1}, and the asymmetrical motion of the Si–O groups at 1074 cm^{-1} [49,56], and after adsorption it will increase to 1083 cm^{-1}.

3.2.4. *Surficial properties of the adsorbents (XPS)*

The chemical element composition of adsorbents was determined by XPS analysis to investigate the phosphate and ammonium adsorption mechanisms. Firstly, as presented in Fig. 8, the survey energy spectra of LMZ exhibited in Fig. 8a show characteristic peaks of P 2p, N 1s, La 3d, and O 1s. After adsorption, Fig. 8b showed a distinct appearance of a new P 2p (132.37 eV), peak. This phenomenon was also observed in the work conducted by Liu et al., 2021 using La modified biochar. In comparison KH_2PO_4 standard P 2p binding energy level (134.0 eV), the P 2p binding energy observed after adsorption was notably decreased, confirming the new phosphate compounds formation [51]. Fig. 8c, showed an enhancement of the N 1s (401.43 eV) peak [53]. These phenomena demonstrated that LMZ was successful in adsorbing phosphate and ammonium. Meanwhile, in Fig. 8, the peaks detected at binding energies of 836.1 and 839.7 eV are associated with $La3d_{5/2}$, while those at 853.0 and 856.8 eV are attributed to $La3d_{3/2}$ [57]. After phosphate adsorption, both the La 3d $_{5/2}$ and La 3d $_{3/2}$ peak positions shifted to higher binding energies. This shift suggests that phosphate ions are directly bound to the La atoms, creating a chemical environment distinct from that of hydroxyl groups [33,50,58].

Fig. 8e shows that the O 1s range of LMZ was divided into three types based on the different binding energies of the various oxides: attached water, or H_2O, matched with 532.01 eV, the metals bounded with compounds (OH-M) to 531.55 eV, and the oxides of metal (M − O) to 530.02 eV. These findings suggested that O–H and O–P exchanged ligands and formation of an inner coordination structure formed in La–O–P. In summary, the removal of ammonium from LMZ may be achieved through ion exchange with La, while the removal of phosphate was achieved by forming La–O–P internal-sphere compound systems, removing hydroxyl atoms via ligand exchange, and electrostatic adsorption [33,50].

A detailed understanding of the solid-water interactions and their mechanisms of the interaction was obtained by comparing the XPS patterns of phoslock, phosphate and ammonium in Fig. S2. As predicted, the survey scan result on the phoslock surface was verified as successful, and phosphate was effectively captured on the adsorbent in Fig. S2a. The newest peak detected in the P 2p spectrum might be attributed to a pair of peaks in Fig. S2b, the P 2p peak value at 133.38 eV and peak P 2p at 132.15 eV, depending on the various forms of the current P elements [59], and the binding energies of the two N 1s peaks Fig. S2c, were 399.33 eV, and 401.66 eV. After adsorption, prominent satellite peaks in the La 3d spectrum underwent a significant energy shift. The vigorous interaction or coordination with the active sites of La and phosphate leads to the development of the bidentate or monodentate La–O–P compound, as seen (in supplementary information of Fig. S2d, [29,53].

Three oxygen species were identified in the high-resolution spectrum of O 1s, such as 530.97 eV (O2−), 531.69 eV (-OH/O–P), and 532.11 eV (H_2O), respectively, in Fig. S2e. Nevertheless, phosphate uptake resulted in a significant energy shift, and this resulted in a decline in the M − OH proportion (M = La). This suggests that phosphate was removed by substituting phosphate anions for –OH, which then allowed for the complexation with metal active sites [29,52]. An XPS investigation was employed to explain the mechanism of phosphate and ammonium adsorption on AA and the findings are displayed in Fig. S3a. In the AA adsorbent XPS full-scan spectra, notable peaks are Al 2p, P 2p, N 1s, and O 1s are evident. The phosphate and ammonium AA XPS full-scan spectrum showed a peak attributed to P 2p when compared to AA before adsorption, indicating that the particles had adsorbed onto the AA. The bind energy peaks of P 2p in Fig. S3b, which are 130.88 eV, and 131.43 eV, indicate the development of an intensely focused interaction between phosphate and the AA adsorbent [26].

In accordance with organic substance XPS, one peak spectrum (after adsorption) at 399.7 in Fig. S3c for N 1s spectra is attributed to an Al–N=N species [60]. In Fig. S3d, it was presented that the spectrum of

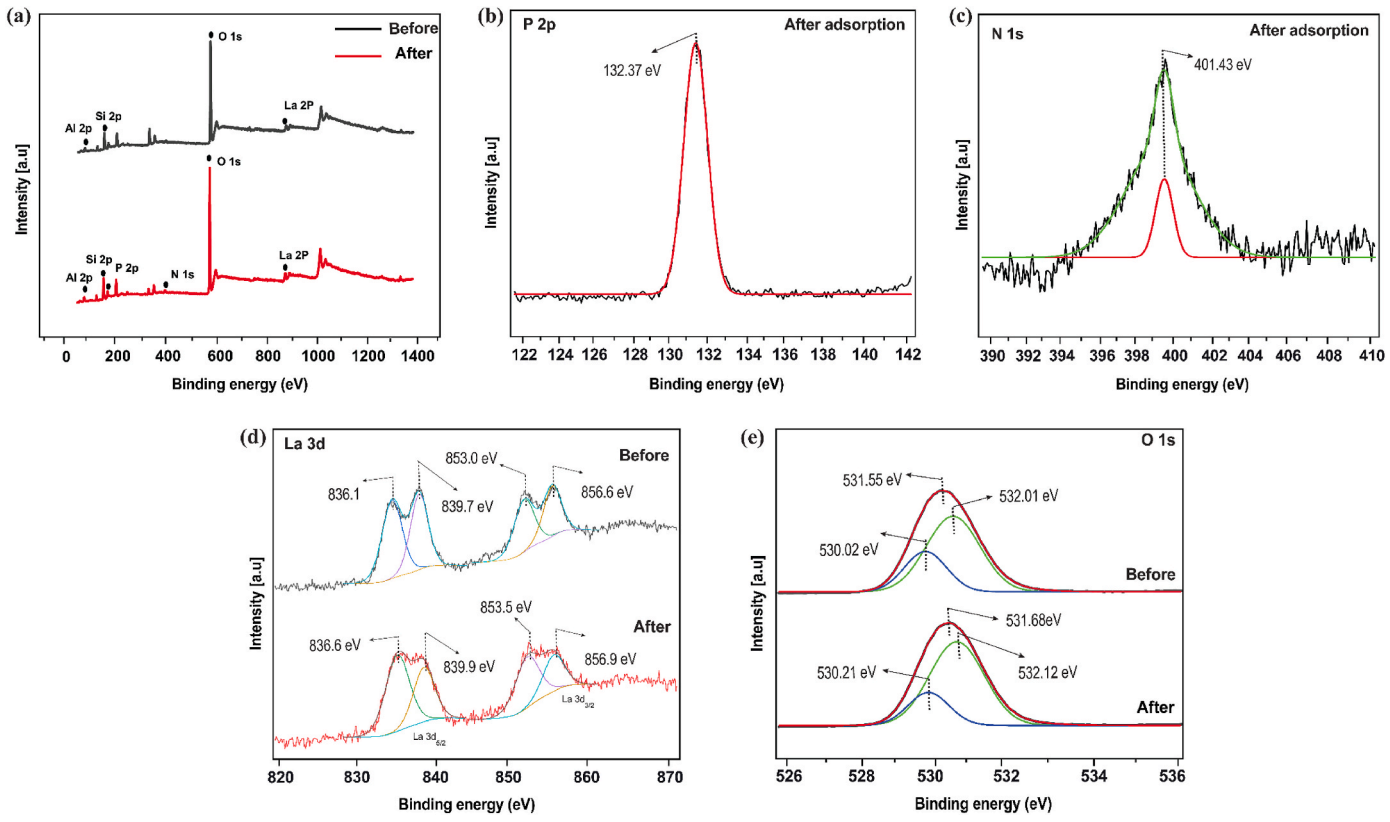

Fig. 8. XPS spectra of LMZ adsorbent before and after (a) wide scan; (b) P 2p; (c) N 1s; (d) La 3d; (e) O 1s.

O 1s XPS can be effectively adapted to the single peak of 531.57 eV, which corresponds to adsorbed H_2O, HO–, and Al–O, respectively [61]. After the adsorption, its binding energy slightly increases to 531.79 eV. The results of the XPS examination indicate the MgFe-BC electronic state transition and the composition of chemical substances during the phosphate and ammonium adsorption processes. The primary constituents of the MgFe-BC before adsorption are C, O, Mg, and Fe, as shown in Fig. S4a.

At the binding energy, a P 2p peak was identified after adsorption, which provided additional evidence of the effective phosphate adsorption. P 2p in Fig. S4b, showed three distinct peaks at 132.78 eV 131.54 eV, and 130.68 eV, in its spectrum. These correspond to HPO_4^{2-}, metal phosphate, and $H_2PO_4^-$, in that order. This demonstrated that phosphate could react with metal on the MgFe-BC, confirming the presence of the interlayer phosphate anion. Fig. S4c illustrates the N chemical bond in the biochar was represented by two peaks in the N 1s region, at binding energies of 398.45 eV and 399.95 eV, ammonium in the double salts, including struvite, and ammonium ions [62] respectively. The spectra of Mg 1s in Fig. S4d illustrate that Mg was also involved in the process of adsorption action at 1304.39 eV and 1306.19 eV, the metal phosphate peak corresponded to a decline in binding energy. Mg 1s spectra presents in the adsorption reaction Mg was also involved, as seen by Fig. S4d, where the binding energy dropped and the peak associated to metal phosphate was seen at 1304.23 eV and 1306.11 eV, respectively.

The O 1s spectrum in Fig. S4e shows that the highest peak value of O 1s in the MgFe-BC separated into peaks representing the binding energy values of 529.18 eV, 531.44 eV, and 531.88 eV prior to the adsorption reaction. The components of these peaks were identified as –OH, attached H_2O, and M − O, which equals M = Mg or Fe [24]. M − O bonding ratio dropped and the OH ratio rose following the adsorption reaction. This was primarily connected to the rehydration reaction of MgFe-BC throughout the process. Several bonds of M − O were converted into the bond of M − OH, which resulted in a decrease in hydroxyl functional groups in metal oxides [63].

In summary, two primary mechanisms that contribute in the ammonium adsorption and process of ammonium on MgFe-BC: electrostatic adsorption and coprecipitation with phosphate to form struvite. Three primary mechanisms underlie the intricate adsorption process of phosphate on MgFe-BC is also electrostatic adsorption and struvite is formed by co-precipitation with ammonium [24,64]. Fig. S5a highlights the DE survey XPS spectrum. In Figs. S5b and c, the DE sample revealed a peak of P 2p and 1 Ns at the binding energies of 130.14 and 400.46 eV, respectively. The peak of Si 2p at 103.67 eV, and an O 1s peak at 531.49 eV are shown in Fig. S5d, [56]. There was no obvious foreign element at the peak. The peak of Si 2p in the Si 2p band spectrum at 103.67 eV represents the atoms of Si in siloxane categories, which are the main component of DE [65], and after the adsorption, oxygen molecules that are part of silicon groups (Si–O–Si) were allocated the binding value of O 1s at 531.68 eV in Fig. S5e [56].

3.3. Adsorption mechanisms

Both adsorption tests and characterization analysis supported the chemisorption of phosphate and ammonium on all adsorbents. Electrostatic attraction was the prevalent mechanism among lanthanum-modified zeolite, phoslock, activated alumina, MgFe-modified biochar, as described in Fig. 9. The SEM images in Fig. 5 indicated LMZ microcube surfaces were covered in flake-like particles after adsorption compare to the pristine LMZ. This change is likely due to the formation of a lanthanum phosphate complex as also reported by Yang et al., [46]. Thus, the key mechanisms for phosphate adsorption were electrostatic attraction and inner sphere complexation through ligand exchange. In a recent work conducted by Yang et al. [15,57], the mechanism of the phosphate adsorption followed similar adsorption behavior as reported in this work, whereas ammonium adsorption was mainly governed by ion exchange. Phoslock utilize inner surface complexation and electrostatic attraction to effectively capture phosphate ions [29]. Activated alumina utilizes ion exchange and electrostatic attraction mechanisms

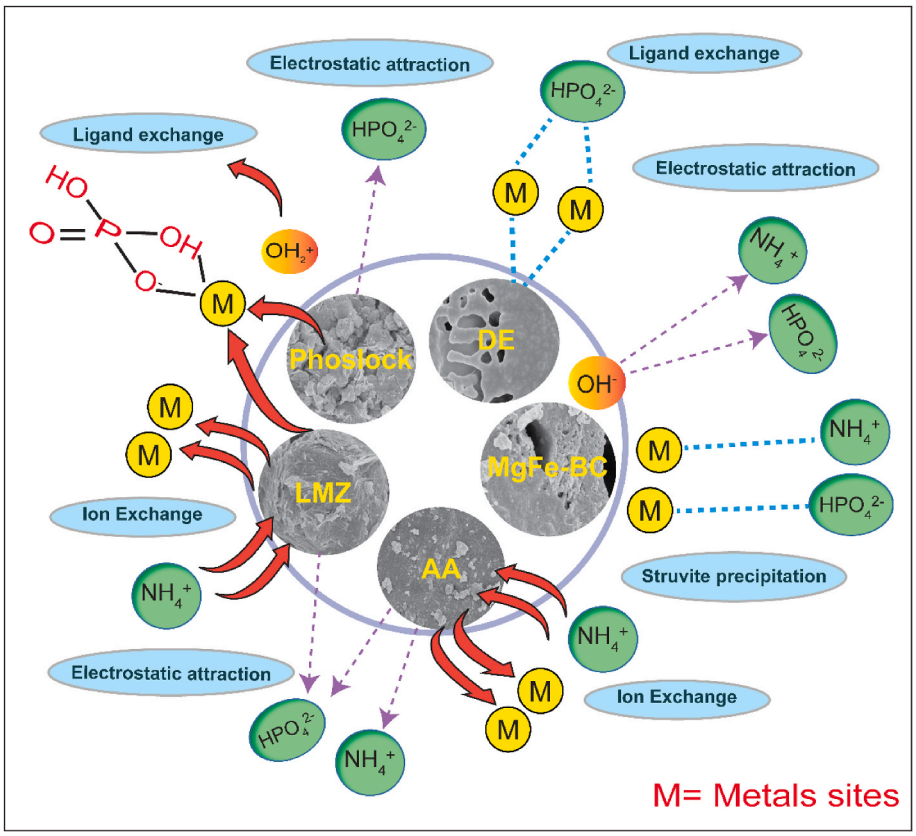

Fig. 9. Adsorption mechanism of phosphate and ammonium by LMZ.

for phosphate adsorption [30], and predominantly electrostatic attraction for ammonium ions [66]. MgFe-modified biochar via electrostatic attraction mechanism adsorb both ammonium and phosphate to initiate the precipitation of struvite [24,64]. Diatomaceous earth, with its porous silica structure, adsorbs phosphate contaminants through ligand exchange as shown in Fig. 9.

3.4. Desorption

Desorption analysis provides a way to assess the stability of LMZ. Three desorption experiments were conducted on LMZ samples previously adsorbed with phosphate and ammonium, with the results depicted in Fig. 10. Phosphate and ammonium desorption behavior as observed by LMZ showed a notable release of these ions during the first desorption phase, which was followed by a progressive reduction in desorption levels with subsequent desorption cycles. The first cycle desorption rates of phosphate and ammonium for LMZ were 63 % and 58 %, respectively, as shown in Fig. 10. According to these results, LMZ appears to have better phosphate and ammonium retention qualities. Significantly, phosphate retention was higher than ammonium retention, suggesting that LMZ is a highly effective phosphate fixer, mostly via chemical adsorption mechanisms [33]. This demonstrates that LMZ has the capacity to firmly bind phosphate ions, which may be advantageous in applications involving water purification.

3.5. Limitations and future works

The current research on simultaneous low-concentration removal of phosphate and ammonium has certain limitations, similar to most studies [67,68]. LMZ is highly effective at simultaneous adsorbing phosphate and ammonium in aquatic systems as compared to other adsorbents, serving to prevent eutrophication. However, its ability to adsorb eutrophic components in realistic environments has not been

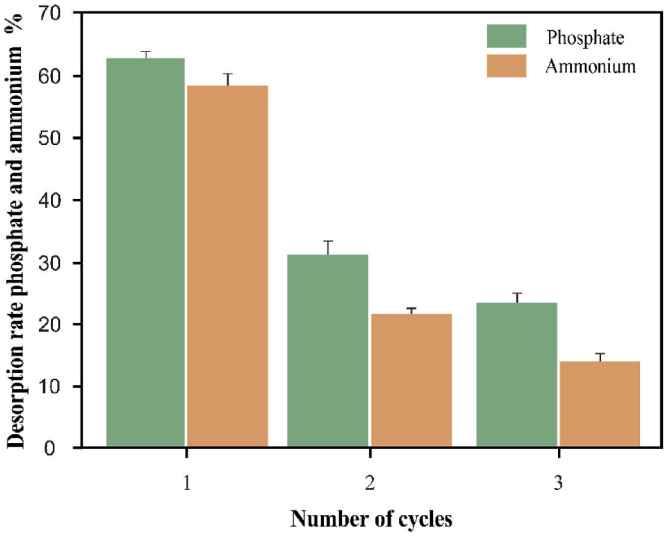

Fig. 10. Desorption efficiency of LMZ through three cycles (*dosage 1 g, time 8 h, initial concentration of phosphate* = 1 mg/L, ammonium = 5 mg/L). Data are provided as mean ± SD (n = 3).

demonstrated. Eutrophic waters present challenges due to its varying pollutant concentrations, intricate water flow patterns, and the presence of additional interfering or coexisting impurities.

4. Conclusion

The present study examines the simultaneous and efficient removal of phosphate and ammonium using variety of absorbents, such as dia-

tomaceous earth, activated alumina, phoslock, and LMZ. Among the adsorbents examined, LMZ revealed remarkable efficiency as an adsorbent, exhibiting dual functionality for effective adsorption of both phosphate and ammonium with 75.4 % and 75.2 % removal, respectively. Moreover, phosphate adsorption capacity was recorded as AA > Phoslock > LMZ > MgFe-BC > DE, while the adsorption capacity for ammonium is LMZ > AA > MgFe-BC > Phoslock > DE. The adsorption isotherm corresponds with Langmuir isotherm equilibrium theory, and kinetic studies indicated that the adsorption process is governed by a PSO exhibited a higher R^2 value as compared to PFO. The effect of adsorbent dosage, initial concentration, co-existing ions, and contact time all had a substantial impact on the pollutants adsorption. Phosphate adsorption was not significantly influenced by the existence of monovalent anions Cl^- or cations K^+, Fe^{3+}, and Na^+ ions. However, it was affected by the involvement of SO_4^{2-}, and CO_3^{2-} ions. Whereas, the presence of Na^+, SO_4^{2-}, and CO_3^{2-}, Cl^- ions showed no effect on ammonium and Fe^{3+}, and K^+ inhibited ammonium adsorption. These five adsorbents in general shows great potential for treating eutrophic water containing phosphate and ammonium at low concentrations and have proven to meet the permissible limit for phosphate and ammonium in river water. The outcomes of this investigation provide a baseline knowledge for estimating and evaluating eutrophic waters and gives critical insight into the concurrent treatment of phosphate and ammonium pollutants at low levels concentrations.

CRediT authorship contribution statement

Uzma Shaheen: Writing – original draft, Methodology, Investigation, Formal analysis, Data curation, Conceptualization, Project administration, Validation, Writing – review & editing. **Zhi-Long Ye:** Writing – review & editing, Supervision, Project administration, Funding acquisition, Conceptualization, Resources. **Olusegun K. Abass:** Writing – review & editing, Methodology, Formal analysis, Supervision. **Doaa Zamel:** Writing – review & editing. **Abdul Rehman:** Writing – review & editing, Software. **Peng Zhao:** Methodology. **Fengming Huang:** Methodology.

Declaration of competing interest

The authors declare that they have no known competing financial interests or personal relationships that could have appeared to influence the work reported in this paper.

Data availability

The authors do not have permission to share data.

Acknowledgments

The funding for this research was supplied by the China Central Government Guided Local Scientific and Technological Development Program of the Fujian Science and Technology Project (No. 2021L3026), the Open Bidding for Selecting the Best Candidates of the IUE Project (IUE-JBGS-202211) and the National Key Research and Development Program (No. 2019YFE0194000) of China.

Appendix A. Supplementary data

Supplementary data to this article can be found online at https://doi.org/10.1016/j.micromeso.2024.113301.

References

[1] C. Takaya, et al., Phosphate and ammonium sorption capacity of biochar and hydrochar from different wastes, Chemosphere 145 (2016) 518–527.
[2] Q. Tang, et al., New strategy to remove phosphate from low concentration solution by MOFs-modified resin: high affinity and thermal desorption, Chem. Eng. J. 465 (2023) 142864.
[3] X. Li, et al., Removal of phosphate at low concentration from water by porous PVA/Al2O3 composites, Environ. Technol. 43 (3) (2022) 345–354.
[4] C. Yunnen, et al., The mechanism of ion exchange and adsorption coexist on medium–low concentration ammonium–nitrogen removal by ion-exchange resin, Environ. Technol. 36 (18) (2015) 2349–2356.
[5] M. Nsenga Kumwimba, et al., Advances in ecotechnological methods for diffuse nutrient pollution control: wicked issues in agricultural and urban watersheds, Front. Environ. Sci. 11 (2023) 1199923.
[6] G. Morse, et al., Phosphorus removal and recovery technologies, Sci. Total Environ. 212 (1) (1998) 69–81.
[7] B. Yuan, et al., Development of a magnetic calcium-alginate hydrogel-sphere encapsulated with Fe–Mn–Zr ternary metal composite for heavy metal adsorption, Sep. Purif. Technol. 306 (2023) 122531.
[8] E. Priya, et al., A comprehensive review on technological advances of adsorption for removing nitrate and phosphate from waste water, J. Water Proc. Eng. 49 (2022) 103159.
[9] T.M. Huggins, et al., Granular biochar compared with activated carbon for wastewater treatment and resource recovery, Water Res. 94 (2016) 225–232.
[10] Y. Yang, et al., Investigation of the key mechanisms and optimum conditions of high-effective phosphate removal by bimetallic La-Fe-CNT film, Sep. Purif. Technol. 341 (2024) 126938.
[11] J. Lin, et al., Removal of phosphate from aqueous solution by a novel Mg (OH) 2/ZrO2 composite: adsorption behavior and mechanism, Colloids Surf. A Physicochem. Eng. Asp. 561 (2019) 301–314.
[12] Y. Yang, et al., Lanthanum carbonate grafted ZSM-5 for superior phosphate uptake: investigation of the growth and adsorption mechanism, Chem. Eng. J. 430 (2022) 133166.
[13] Y. Chen, et al., Removal and recovery of phosphate anion as struvite from wastewater, Clean Technol. Environ. Policy 20 (2018) 2375–2380.
[14] T. Fan, et al., Experimental study of the adsorption of nitrogen and phosphorus by natural clay minerals, Adsorpt. Sci. Technol. 2021 (2021) 1–14.
[15] Y. Yang, et al., Mechanistic study of highly effective phosphate removal from aqueous solutions over a new lanthanum carbonate fabricated carbon nanotube film, J. Environ. Manag. 359 (2024) 120938.
[16] S. Pourshadlou, et al., Facile preparation of bentonite/nano-gamma alumina composite as a cost-effective adsorbent for Ca2+ removal from aqueous solutions, J. Ind. Eng. Chem. 127 (2023) 496–508.
[17] N. Sankararamakrishnan, M. Jaiswal, N. Verma, Composite nanofloral clusters of carbon nanotubes and activated alumina: an efficient sorbent for heavy metal removal, Chem. Eng. J. 235 (2014) 1–9.
[18] M. Bassyouni, et al., Utilization of carbon nanotubes in removal of heavy metals from wastewater: a review of the CNTs' potential and current challenges, Appl. Phys. A 126 (2020) 1–33.
[19] M.M. Sabzehmeidani, et al., Carbon based materials: a review of adsorbents for inorganic and organic compounds, Materials Advances 2 (2) (2021) 598–627.
[20] D. Guaya, et al., Modification of a natural zeolite with Fe (III) for simultaneous phosphate and ammonium removal from aqueous solutions, J. Chem. Technol. Biotechnol. 91 (6) (2016) 1737–1746.
[21] M. Rouhani, et al., Evaluation of tetracycline removal by adsorption method using magnetic iron oxide nanoparticles (Fe3O4) and clinoptilolite from aqueous solutions, J. Mol. Liq. 356 (2022) 119040.
[22] A. Rasaie, et al., Removal of herbicide paraquat from aqueous solutions by bentonite modified with mesoporous silica, Mater. Chem. Phys. 262 (2021) 124296.
[23] Y. He, et al., Simultaneous removal of ammonium and phosphate by alkaline-activated and lanthanum-impregnated zeolite, Chemosphere 164 (2016) 387–395.
[24] H. Liu, et al., Efficient recovery of phosphate from simulated urine by Mg/Fe bimetallic oxide modified biochar as a potential resource, Sci. Total Environ. 784 (2021) 147546.
[25] C. Fang, et al., Phosphorus recovery from biogas fermentation liquid by Ca–Mg loaded biochar, J. Environ. Sci. 29 (2015) 106–114.
[26] J. Sun, et al., Removal of phosphorus from wastewater by different morphological alumina, Molecules 25 (13) (2020) 3092.
[27] Q. Yin, et al., Computational study of phosphate adsorption on Mg/Ca modified biochar structure in aqueous solution, Chemosphere 269 (2021) 129374.
[28] V.T. Trinh, et al., Phosphate adsorption by silver nanoparticles-loaded activated carbon derived from tea residue, Sci. Rep. 10 (1) (2020) 3634.
[29] B. Wang, et al., Efficient phosphate elimination from aqueous media by La/Fe bimetallic modified bentonite: adsorption behavior and inner mechanism, Chemosphere 312 (2023) 137149.
[30] M.N. Afridi, J. Lee, J. Kim, Recovery of phosphate from wastewater using alumina nanotubes, Desalination Water Treat. 144 (2019) 355–369.
[31] H. Li, et al., Efficient simultaneous phosphate and ammonia adsorption using magnesium-modified biochar beads and their recovery performance, J. Environ. Chem. Eng. 11 (5) (2023) 110875.
[32] X.F. Xie FaZhi, et al., Phosphorus Removal from Eutrophic Waters with a Novel Lanthanum-Modified Diatomite, 2013.
[33] W. Sang, et al., Na@ La-modified zeolite particles for simultaneous removal of ammonia nitrogen and phosphate from rejected water: performance and mechanism, Water Sci. Technol. 82 (12) (2020) 2975–2989.
[34] B. Wang, et al., La/Al engineered bentonite composite for efficient phosphate separation from aqueous media: preparation optimization, adsorptive behavior and mechanism insight, Sep. Purif. Technol. 290 (2022) 120894.

[35] K. Wu, et al., Evaluation of the adsorption of ammonium-nitrogen and phosphate on a granular composite adsorbent derived from zeolite, Environ. Sci. Pollut. Control Ser. 26 (2019) 17632–17643.
[36] M. Wang, et al., A novel mesoporous zeolite-activated carbon composite as an effective adsorbent for removal of ammonia-nitrogen and methylene blue from aqueous solution, Bioresour. Technol. 268 (2018) 726–732.
[37] Q. Cheng, et al., Study on the adsorption of nitrogen and phosphorus from biogas slurry by NaCl-modified zeolite, PLoS One 12 (5) (2017) e0176109.
[38] M. Nehra, et al., Metal organic frameworks MIL-100 (Fe) as an efficient adsorptive material for phosphate management, Environ. Res. 169 (2019) 229–236.
[39] M.N. Afridi, W.-H. Lee, J.-O. Kim, Application of synthesized bovine serum albumin-magnetic iron oxide for phosphate recovery, J. Ind. Eng. Chem. 86 (2020) 113–122.
[40] H. Li, et al., An investigation into the rapid removal of tetracycline using multilayered graphene-phase biochar derived from waste chicken feather, Sci. Total Environ. 603 (2017) 39–48.
[41] F. Reguyal, A.K. Sarmah, Site energy distribution analysis and influence of Fe3O4 nanoparticles on sulfamethoxazole sorption in aqueous solution by magnetic pine sawdust biochar, Environ. Pollut. 233 (2018) 510–519.
[42] J. Yu, et al., Enhanced removal of Cr (VI) from aqueous solution by supported ZnO nanoparticles on biochar derived from waste water hyacinth, Chemosphere 195 (2018) 632–640.
[43] R. Liu, et al., Simultaneous removal of ammonium and phosphate in aqueous solution using Chinese herbal medicine residues: mechanism and practical performance, J. Clean. Prod. 313 (2021) 127945.
[44] Y.-H. Jiang, et al., Characteristics of nitrogen and phosphorus adsorption by Mg-loaded biochar from different feedstocks, Bioresour. Technol. 276 (2019) 183–189.
[45] N. Cheng, et al., Co-adsorption performance and mechanism of nitrogen and phosphorus onto eupatorium adenophorum biochar in water, Bioresour. Technol. 340 (2021) 125696.
[46] Y. Yang, et al., An innovative lanthanum carbonate grafted microfibrous composite for phosphate adsorption in wastewater, J. Hazard Mater. 392 (2020) 121952.
[47] K.Y. Koh, S. Zhang, J.P. Chen, Hydrothermally synthesized lanthanum carbonate nanorod for adsorption of phosphorus: material synthesis and optimization, and demonstration of excellent performance, Chem. Eng. J. 380 (2020) 122153.
[48] X. Tao, T. Huang, B. Lv, Synthesis of Fe/Mg-biochar nanocomposites for phosphate removal, Materials 13 (4) (2020) 816.
[49] N.A. Fathy, et al., Strengthening the surface and adsorption properties of diatomite for removal of Cr (VI) and methylene blue dye, Arabian J. Geosci. 15 (22) (2022) 1664.
[50] R. Yang, et al., Performance and mechanism of lanthanum-modified zeolite as a highly efficient adsorbent for fluoride removal from water, Chemosphere 307 (2022) 136063.
[51] L. Liu, et al., Phosphate adsorption characteristics of La (OH) 3-modified, canna-derived biochar, Chemosphere 286 (2022) 131773.
[52] Q. Song, et al., Synthesis of magnetite/lanthanum hydroxide composite and magnetite/aluminum hydroxide composite for removal of phosphate, Sci. Total Environ. 723 (2020) 137838.
[53] M. Zhang, et al., Characteristics and mechanism of phosphate removal by lanthanum modified bentonite in the presence of dissolved organic matter, Chemosphere 340 (2023) 139957.
[54] H. Bian, et al., MgFe-LDH@ biochars for removing ammonia nitrogen and phosphorus from biogas slurry: synthesis routes, composite performance, and adsorption mechanisms, Chemosphere 324 (2023) 138333.
[55] H. Bian, et al., An improved method of MgFe-layered double hydroxide/biochar composite synthesis, J. Clean. Prod. 393 (2023) 136186.
[56] M.B. Nguyen, et al., High CO adsorption performance of CuCl-modified diatomites by using the novel method “atomic implantation”, J. Chem. 2021 (2021) 1–12.
[57] Y. Yang, et al., Construction of a novel lanthanum carbonate-grafted ZSM-5 zeolite for effective highly selective phosphate removal from wastewater, Microporous Mesoporous Mater. 324 (2021) 111289.
[58] Q. Luo, et al., High-efficiency lanthanum-modified zeolite adsorbents for phosphorus control and algal suppression: preparation, characterization and mechanistic insights, Sep. Purif. Technol. 352 (2024) 128146.
[59] B. Wang, et al., Novel talc encapsulated lanthanum alginate hydrogel for efficient phosphate adsorption and fixation, Chemosphere 256 (2020) 127124.
[60] C. Soto, V. Boiadjiev, W. Tysoe, Spectroscopic study of AlN film formation by the sequential reaction of ammonia and trimethylaluminum on alumina, Chem. Mater. 8 (9) (1996) 2359–2365.
[61] B. Wang, et al., Adsorption performance and mechanism of mesoporous carbon-doped Al2O3 adsorbent derived from NH2-MIL-53 (Al) for removing Cr (VI) and methyl orange from aqueous solution, J. Environ. Chem. Eng. 11 (3) (2023) 110081.
[62] G. Cai, Z.-l. Ye, Concentration-dependent adsorption behaviors and mechanisms for ammonium and phosphate removal by optimized Mg-impregnated biochar, J. Clean. Prod. 349 (2022) 131453.
[63] M. Mallet, et al., Investigation of phosphate adsorption onto ferrihydrite by X-ray photoelectron spectroscopy, J. Colloid Interface Sci. 407 (2013) 95–101.
[64] X. Wu, et al., Efficient adsorption of nitrogen and phosphorus in wastewater by biochar, Molecules 29 (5) (2024) 1005.
[65] F. Lamastra, et al., A new green methodology for surface modification of diatomite filler in elastomers, Mater. Chem. Phys. 194 (2017) 253–260.
[66] C. Yeom, Y. Kim, Adsorption of ammonia using mesoporous alumina prepared by a templating method, Environmental Engineering Research 22 (4) (2017) 401–406.
[67] S. Sengupta, T. Nawaz, J. Beaudry, Nitrogen and phosphorus recovery from wastewater, Current Pollution Reports 1 (2015) 155–166.
[68] X. Ma, et al., Simultaneous adsorption of ammonia and phosphate using ferric sulfate modified carbon/zeolite composite from coal gasification slag, J. Environ. Manag. 305 (2022) 114404.